

JGR Space Physics

RESEARCH ARTICLE

10.1029/2023JA032249

A New Model of Electron Pitch Angle Distributions and Loss Timescales in the Earth's Radiation Belts

S. A. Glauert¹ , J. W. Atkinson^{1,2} , J. P. Ross¹ , and R. B. Horne¹ 

¹British Antarctic Survey, Cambridge, UK, ²University of Cambridge, Cambridge, UK

Key Points:

- The combined effect of all the VLF waves that typically interact with radiation belt electrons is included in the calculations
- When chorus is the dominant wave pitch angle distributions show little activity dependence, unlike the corresponding loss timescales
- Increasing geomagnetic activity tends to broaden the peak of the distributions dominated by hiss and narrow those dominated by EMIC waves

Correspondence to:

S. A. Glauert,
sagl@bas.ac.uk

Citation:

Glauert, S. A., Atkinson, J. W., Ross, J. P., & Horne, R. B. (2024). A new model of electron pitch angle distributions and loss timescales in the earth's radiation belts. *Journal of Geophysical Research: Space Physics*, 129, e2023JA032249. <https://doi.org/10.1029/2023JA032249>

Received 3 NOV 2023

Accepted 14 MAY 2024

Abstract As the number of satellites on orbit grows it is increasingly important to understand their operating environment. Physics-based models can simulate the behavior of the Earth's radiation belts by solving a Fokker-Planck equation. Three-dimensional models use diffusion coefficients to represent the interactions between electromagnetic waves and the electrons. One-dimensional radial diffusion models neglect the effects of energy diffusion and represent the losses due to the waves with a loss timescale. Both approaches may use pitch angle distributions (PADs) to create boundary conditions, to map observations from low to high equatorial pitch angles and to calculate phase-space density from observations. We present a comprehensive set of consistent PADs and loss timescales for $2 \leq L^* \leq 7$, $100 \text{ keV} \leq E \leq 5 \text{ MeV}$ and all levels of geomagnetic activity determined by the Kp index. These are calculated from drift-averaged diffusion coefficients that represent all the VLF waves that typically interact with radiation belt electrons and show good agreement with data. The contribution of individual waves is demonstrated; magnetosonic waves have little effect on loss timescales when lightning-generated whistlers are present, and chorus waves contribute to loss even in low levels of geomagnetic activity. The PADs vary in shape depending on the dominant waves. When chorus is dominant the distributions have little activity dependence, unlike the corresponding loss timescales. Distributions peaked near 90° are formed by plasmaspheric hiss for $L^* \leq 3$ and $E < 1 \text{ MeV}$, and by EMIC waves for $L^* > 3$ and $E > 1 \text{ MeV}$. When hiss dominates, increasing activity broadens the distribution but when EMIC waves dominate increasing activity narrows the distribution.

Plain Language Summary As the number of satellites on orbit grows it is increasingly important to understand their operating environment. Physics-based models of the radiation belts can be used to model how the radiation environment varies with time. Three-dimensional models typically include the effect of interactions between electromagnetic waves and electrons in the belts on both the motion and energy of the electrons. One-dimensional models simplify the modeling by neglecting the effect of the waves on the energy of the electron and only consider how rapidly they are lost. Both types of model require an understanding of how electrons are distributed in the belts and how they are lost. We present calculations of the timescale for electron loss from the belts and for the shape of the distribution of electrons with equatorial pitch angle, a variable related to latitude, due to the combined effect of all the VLF waves that typically interact with radiation belt electrons. Our results show good agreement with the observations. They vary significantly with location, energy and geomagnetic activity, the influence of individual waves can be identified, and the model provides a useful resource for radiation belt models.

1. Introduction

The Earth is surrounded by the Van Allen radiation belts; regions of space where energetic charged particles are trapped by the Earth's magnetic field. Electrons normally form two torus-shaped belts around the Earth and the outer belt in particular is highly variable, especially during geomagnetic storms, for example, (Baker et al., 1997; Reeves et al., 2003, 2016). This variability is the result of the interaction of a variety of processes such as radial transport, wave-particle interactions, injections from the plasma sheet and loss to the atmosphere and magnetopause. Understanding the effects of these processes on the radiation belts is important as the radiation can pose a hazard to spacecraft (Baker, 2001; Horne & Pitchford, 2015; Wrenn et al., 2002).

Wave-particle interactions are a significant contributor to the variability of the radiation belts (Horne et al., 2016; Horne & Thorne, 1998; Jaynes et al., 2015), so quantitative assessment of their effects is important for accurate modeling, and ultimately forecasting, of the radiation belts. Using quasi-linear diffusion theory (Kennel & Engelmann, 1966; Lyons, 1974), diffusion coefficients that describe the resonant interaction between electrons

©2024. The Author(s).

This is an open access article under the terms of the [Creative Commons Attribution License](https://creativecommons.org/licenses/by/4.0/), which permits use, distribution and reproduction in any medium, provided the original work is properly cited.

and electromagnetic waves present in space can be determined (Glauert & Horne, 2005). These diffusion coefficients can be incorporated directly into 3-dimensional radiation belt models (Albert et al., 2009; Glauert et al., 2014b; Subbotin et al., 2010; Tu et al., 2013). They can also be used to derive pitch angle distributions (PADs) that are widely used in radiation belt modeling. PADs are required, for example, when mapping observations made at low equatorial pitch-angles to higher equatorial pitch angles (Allison et al., 2018), or to impose initial and boundary conditions at all pitch angles from an observation that does not have pitch angle resolution (Glauert et al., 2018). Diffusion coefficients can also be used to determine theoretical electron loss timescales for use in simpler, but faster, 1-dimensional radial diffusion models (Ozeke et al., 2018; Shprits & Thorne, 2004; Summers et al., 2002). This paper presents theoretical PADs and the associated loss timescales for the combined effect of the very low frequency (VLF) waves most commonly associated with wave-particle interactions in the radiation belts.

PADs and loss timescales can be derived directly from pitch angle diffusion coefficients (Albert, 1994; Lyons et al., 1972), by assuming pitch angle diffusion is the dominant process and that the phase-space density can be factorized into time dependent and pitch angle dependent functions. The PAD is then the solution of an integral equation and the associated loss timescale can be derived from the derivative of the distribution. Although this approach neglects the effects of other processes, such as radial or energy diffusion, it has the advantage that it can provide PADs and loss timescales for active conditions, which can be more challenging for observation based approaches to estimating them. Also, by using drift-averaged diffusion coefficients, drift-averaged PADs and loss timescales can be obtained for use in 3-dimensional radiation belt modeling.

The Lyons et al. (1972) and Albert (1994) approaches have not been widely employed to derive PAD models from diffusion coefficients. However, several authors have developed empirical models of the dependence of pitch angle distributions on energy, location and geomagnetic activity. Chen et al. (2014) fitted Legendre polynomials to data from the Combined Release and Radiation Effects Satellite (CRRES), Global Geospace Science Polar Satellite (Polar) and a Los Alamos National Laboratory geosynchronous satellite (LANL-97A). Their model covered L-shells from 3.0 to 9.0, energies from 148 keV to 1.58 MeV and used the AE index to determine geomagnetic activity. Shi et al. (2016) assumed the pitch angle distribution behaved as $\sin^n \alpha$, where α is local pitch angle, and used Van Allen Probes data to determine n for a range of energies ($100 \text{ keV} \leq E \leq 1 \text{ MeV}$) and L-shell ($1.1 \leq L \leq 6.1$) with geomagnetic conditions determined by the Kp index. Zhao et al. (2018) also fitted Legendre polynomials to VAP data to provide PADs for electron energies from 30 keV to 5.2 MeV and L-shells from 1 to 6 with geomagnetic activity determined by Dst. Allison et al. (2018) fitted a double sin function to VAP data, parameterized by L^* and Kp, as the results were used to derive boundary conditions for a radiation belt model. The resulting PAD model covered energies from 100 to 800 keV for $1.5 \leq L^* \leq 5.9$ with three Kp bands. Smirnov et al. (2022) also used VAP data and fitted fifth order Fourier series to the PADs for $1.2 \leq L \leq 5.7$ and energies between 30 keV and 1.65 MeV, for different levels of solar wind pressure.

Although each of these studies provides useful information about the PADs, no individual study covers the range of L^* (at least $2 \leq L^* \leq 7$) and energies (100 keV to multi-MeV) that may be required in radiation belt modeling. Combining the various studies is complicated by the different choices for activity index made by the different authors. Also, most of these studies (Allison et al. (2018) is the exception) are parameterized by the McIlwain L-shell parameter, whereas radiation belt models typically use the Roederer L^* parameter (Roederer, 1970), proportional to the inverse of the third adiabatic invariant, which can differ significantly from L-shell in a non-dipole field. Radiation belt models assume that electrons drift around the Earth at a fixed value of L^* . A drift-averaged PAD derived at a fixed value of L-shell will sample a range of L^* values and may be different to the distribution at the corresponding value of L^* .

Several types of PAD are commonly seen in the radiation belts (see e.g., Chen et al. (2014)). Flat top PADS have a low flux at the loss cone but a near-constant flux over the higher pitch angles. Pancake distributions have a peak at 90° , while butterfly PADs have a local minimum at 90° with a maximum at a lower pitch angle above the loss cone.

Unlike the PADs, various authors have created theoretical models of electron loss timescales from diffusion coefficients, for example, Aryan et al. (2020); Claudepierre et al. (2020a); Gu et al. (2012); Orlova and Shprits (2014); Orlova et al. (2016); Shprits et al. (2007). However, these typically employ an approximation to derive the loss timescale using results from Shprits et al. (2006) or Albert and Shprits (2009), and so do not provide an associated PAD. Most of these models are also limited to a single wave mode, restricting their

usability, as the combined effect of two wave-modes cannot always be obtained by combining their individual loss timescales (Meredith et al., 2006). However, Claudepierre et al. (2020a) do consider the combined effect of several different waves and calculate loss timescales for a combination of plasmaspheric hiss, VLF transmitters, lightning-generated whistlers (LGW), electromagnetic ion cyclotron (EMIC) waves and collisions with the atmosphere, providing loss timescales for $1 \leq L \leq 6$ and energies from 0.1 keV to 10 MeV, parameterized by Kp.

Many authors have derived electron decay timescales from observations, either focusing on specific waves modes (Meredith et al., 2006; Orlova & Shprits, 2014) or treating the decay more generally (Baker et al., 2007; Claudepierre et al., 2020a; Meredith et al., 2009; Ripoll et al., 2015). These estimates tend to focus on sustained periods of decay and so are most applicable to quiet or moderate levels of geomagnetic activity. Also, they can only be made for regions, time periods and energies where sufficient observations exist and so they may not cover the whole domain of a model simulation. Additionally, it may be difficult to isolate the effects due to particular waves from other processes (e.g., radial diffusion) occurring simultaneously in the radiation belts and, like PADs, these empirical loss timescales are mainly presented in terms of the L-shell rather than L^* .

The main motivation for the work presented here is the need for PADs to create boundary conditions for radiation belt modeling and forecasting. The distributions are required to map Low Earth Orbit (LEO) electron flux observations from the observed low equatorial pitch angles to the magnetic equator, and for deriving pitch angle distributions from omni-directional observations, such as those provided by GPS satellites. The aim is to provide a model, parameterized by Kp, that covers the extensive L^* ($2 \leq L^* \leq 7$) and energy (100 keV to multi-MeV energies) ranges that can be used in radiation belt modeling. The Kp index has been used to determine geomagnetic activity because it is the only activity index that is common to all the diffusion models used in the study and also because the pitch angle distributions will be used in Sat-Risk project (<https://sat-risk.ac.uk>) developing radiation belt forecasts at the Met Office, where Kp is the only index that is available for the forecast. The creation of a comprehensive set of electron loss timescales for use in radial diffusion models provided additional motivation for the work.

The results presented here provide PADs and loss timescales for the combined effects of upper and lower band chorus, plasmaspheric hiss, lightning-generated whistlers, VLF transmitters, magnetosonic waves, electromagnetic ion cyclotron (EMIC) waves and collisions with the atmosphere. Section 2 describes the calculation of the PADs and loss timescales and the diffusion coefficients that were used to derive them. The electron loss timescales are presented and compared to observations in Section 3. Section 4 describes the associated PADs and compares them to empirical results. A discussion of the results and their limitations is presented in Section 5 and our conclusions are summarized in Section 6.

2. Calculation of Loss Timescales and Pitch Angle Distributions

The behavior of high-energy electrons in the radiation belt is typically modeled by a diffusion equation (Schulz & Lanzerotti, 1974). Assuming pure pitch angle diffusion, ignoring any contribution from energy and radial diffusion, the evolution of the bounce- and drift-averaged phase space density $f(\alpha_0, t)$ for a given energy (E) and L^* , is given by

$$\frac{\partial f}{\partial t} = \frac{1}{T(\alpha_0) \sin(2\alpha_0)} \frac{\partial}{\partial \alpha_0} \bigg|_{L^*, E} \left(T(\alpha_0) \sin(2\alpha_0) D_{\alpha\alpha} \frac{\partial f}{\partial \alpha_0} \right) \quad (1)$$

Here α_0 is the equatorial pitch angle, $T(\alpha_0) \approx 1.30 - 0.56 \sin \alpha_0$ is the normalized electron bounce period in a dipole field (Schulz & Lanzerotti, 1974), and $D_{\alpha\alpha}(\alpha_0, E, L^*, I)$ is the drift- and bounce averaged diffusion coefficient for the given equatorial pitch angle, energy, L^* and I , a geomagnetic activity index.

Following Lyons et al. (1972), assume $f = g(\alpha_0) e^{-t/\tau}$ for some pitch angle distribution, $g(\alpha_0)$, and electron loss timescale, τ , then

$$\frac{d}{d\alpha_0} \left(D_{\alpha\alpha} T \sin(2\alpha_0) \frac{dg}{d\alpha_0} \right) + \frac{T \sin(2\alpha_0)}{\tau} g = 0. \quad (2)$$

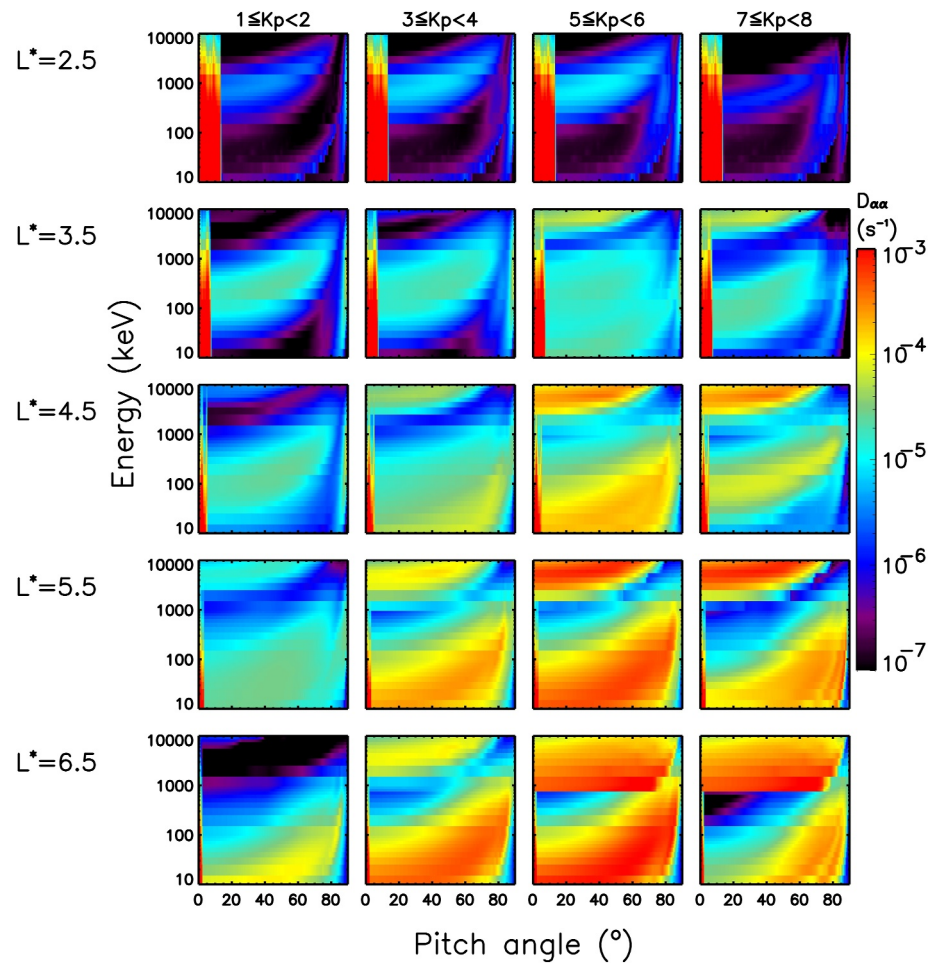


Figure 1. Combined pitch angle diffusion coefficients for chorus, hiss, lightning-generated whistlers, transmitters, magnetosonic, EMIC waves and collisions for the indicated values of L^* and activity defined by the Kp index.

Albert (1994) shows the solution of this equation for the PAD and loss timescale, with the appropriate boundary conditions, can be reformulated as a boundary value problem involving a set of four ordinary differential equations with appropriate boundary conditions. This approach was followed to calculate the results presented here, as described in Meredith et al. (2006).

The boundary conditions require the pitch angle distribution to be normalized and to be symmetric about $\alpha_0 = 90^\circ$. Additionally, Lyons et al. (1972) and Albert (1994) set the phase-space density to zero at the edge of the loss cone. However, since measurements made at LEO may be partially within the loss cone, for the applications envisioned here there is an advantage in obtaining a pitch angle distribution that extends into the loss cone. To achieve this, the lower pitch angle boundary condition is $f = 0$ at $\alpha_0 = 1.0^\circ$, and pitch angle diffusion due to collisions is included in the calculation, since this diffusion is very rapid (see Figure 1) within the loss cone.

The final result from these calculations is a normalized pitch angle distribution of phase-space density as a function of equatorial pitch angle with a corresponding loss timescale, τ , for each L^* , energy and geomagnetic activity level.

2.1. Diffusion Coefficients

The diffusion coefficients used in this study represent the main types of gyro-resonant VLF wave particle interactions found in the magnetosphere; plasmaspheric hiss, upper and lower band chorus waves, EMIC waves, VLF transmitters, lightning-generated whistlers (LGW) and magnetosonic waves. All are derived from

observations using the Olson-Pfizer field model (Olson & Pfizer, 1977), are bounce- and drift-averaged and use K_p to determine the level of geomagnetic activity.

The diffusion coefficients for the pitch angle diffusion due to plasmaspheric hiss are those used in Glauert et al. (2021), calculated using the wave models from Meredith et al. (2018), and are defined for $2 \leq L^* \leq 6$. Those for chorus are calculated using the observations in Meredith et al. (2020) and the PADIE code (Glauert & Horne, 2005), as in Reidy et al. (2021), and cover the range $2 \leq L^* \leq 10$. For VLF transmitters, the diffusion coefficients are defined for $L^* \leq 3$ and are taken from Ross et al. (2019). The diffusion coefficients for EMIC waves are given in Ross et al. (2021) for $3.25 \leq L^* \leq 5.25$ and in Ross et al. (2020) for $5.25 < L^* \leq 7$. For LGW the diffusion coefficients were calculated by the PADIE code (Glauert & Horne, 2005) using the wave models from Green et al. (2020) and the density model from (Ozhogin et al., 2012) and cover $2 \leq L^* \leq 3$. The Green et al. (2020) wave models were derived in L-shell, not L^* , so it has been assumed that $L = L^*$. This is a reasonable approximation as LGW are only included for low L-shells, where a dipole is a good approximation to the magnetic field and L-shell and L^* are equal in a dipole. The diffusion coefficients for magnetosonic waves are from Wong et al. (2022) and defined for $2 \leq L^* \leq 6$. As well as these contributions due to the waves, the pitch angle diffusion due to collisions with the atmosphere is also included following the method in Selesnick (2016), assuming an eccentric tilted dipole for the magnetic field, and again that $L = L^*$.

The pitch angle diffusion coefficients for the different waves are defined on a number of different pitch angle, energy, L^* and K_p grids. To combine them the diffusion coefficients for each wave were interpolated to a fixed pitch angle (every 0.5°), energy (10, 20, ..., 90, 100, 200, ..., 900 keV, 1, 2, ..., 5 MeV) and L^* (2, 2.5, ..., 7) grid and then binned into activity bins $0 \leq K_p < 1$, $1 \leq K_p < 2$ etc. Figure 1 shows the combined diffusion coefficients for a range of energies, L^* , and activity levels. At low L^* ($L^* \leq 3$) and activity the main contribution to diffusion outside of the loss cone comes from plasmaspheric hiss, with additional contributions from transmitters and LGW. Inside the loss cone diffusion is dominated by collisions with very large values of $D_{\alpha\alpha}$. The effects of chorus become dominant as activity increases, particularly at lower (<1 MeV) energies and higher L^* , whilst the contribution from EMIC waves is apparent at MeV energies and lower pitch angles for $L^* \geq 3.25$.

3. Electron Loss Timescales

The diffusion coefficients in Figure 1 were used to determine PADs and loss timescales using the approach outlined above. These were calculated for energies from 100 keV to 5 MeV with the same L^* and activity resolution as the diffusion coefficients.

Claudepierre et al. (2020a) used Van Allen Probes data to derive loss timescales for different energy electrons during extended periods of decay. Some of these results are reproduced in Figure 2. Each panel corresponds to a different energy (102, 350, 467, 743, 1,010 and 2,600 keV) indicated in the title, and the solid black lines are the Claudepierre et al. (2020a) median loss timescales as a function of L^* . The shaded areas show their maximum and minimum values. The upper and lower dotted gray lines show the theoretical loss timescales calculated from their diffusion coefficients by Claudepierre et al. (2020b) for $K_p = 0$ and $K_p = 5$ respectively.

The red, blue and green lines show loss timescales calculated from the diffusion coefficients in Figure 1 for $0 \leq K_p < 1$, $2 \leq K_p < 3$ and $4 \leq K_p < 5$, respectively. The energies at which the diffusion coefficients are calculated, and hence the PADs and loss timescales, are not the same as the energies for which the Claudepierre data in Figure 2 is available. To make the comparison in Figure 2, the loss timescales calculated from the diffusion coefficients in Figure 1 are for the nearest available energies (100, 300, 500, 700 keV, 1 and 3 MeV).

The Claudepierre et al. (2020b) empirical loss timescales were derived from periods where the fluxes were decreasing for at least 5 days, which typically occur during low geomagnetic activity, so direct comparisons between the empirical loss timescales and the results presented here should focus on the $0 \leq K_p < 1$ (red) and $2 \leq K_p < 3$ (blue) results. Claudepierre et al. (2020a) give the mean K_p for the decay periods as $K_p = 2$. The green curves represent more active conditions ($4 \leq K_p < 5$), and are provided as an illustration of the effect of more active conditions. Also, note that the Claudepierre et al. (2020b) results were derived in McIlwain L-shell rather than L^* . At the low levels of activity represented in the Claudepierre data differences are unlikely to be significant at low L-shell or L^* , but the higher L-shells may correspond to slightly lower L^* . As the empirical loss timescales tend to be relatively flat at higher L^* (except for 2.6 MeV), this is unlikely to significantly affect the comparisons.

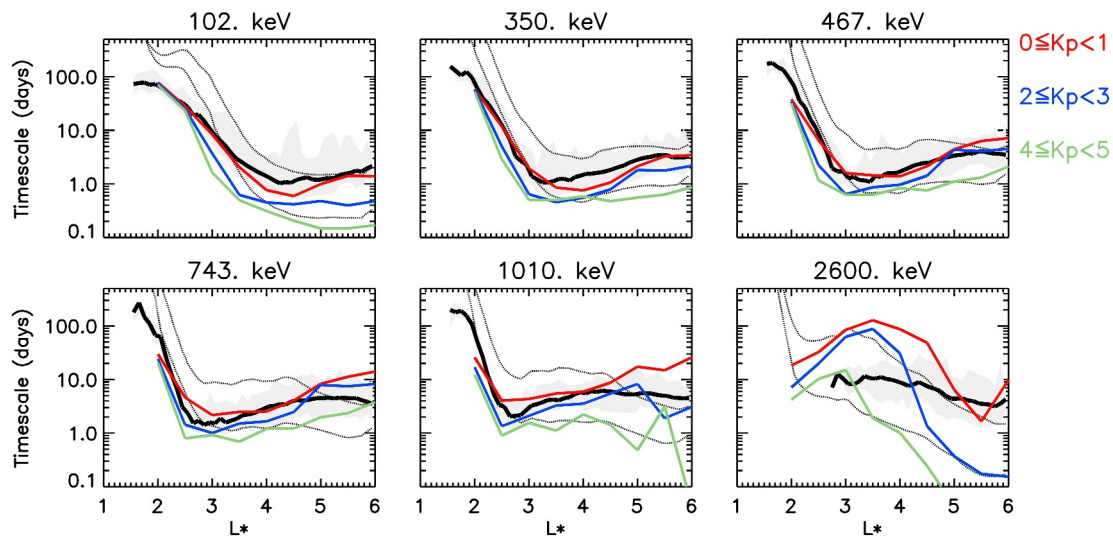


Figure 2. Electron loss timescales as a function of L^* for selected energies and activity levels. The red, blue and green lines are the loss timescales calculated using the diffusion coefficients from Figure 1 for $0 \leq Kp < 1$, $2 \leq Kp < 3$ and $4 \leq Kp < 5$ respectively. The solid black lines are loss timescales derived from VAP observations by Claudepierre et al. (2020b). The upper and lower gray dotted lines are loss timescales calculated from diffusion coefficients by Claudepierre et al. (2020a) for $Kp = 0$ and 5 respectively.

Generally, there is good agreement between the $0 \leq Kp < 1$ (red) and $2 \leq Kp < 3$ (blue) results and the data, especially for energies below 1 MeV where the loss timescales for low activity generally lie close to the data and within the range of observations. As would be expected, the loss timescales for the higher level of activity ($4 \leq Kp < 5$) are generally shorter, especially at the higher L^* , where chorus waves are more significant. For $L^* < 3$ the calculated loss timescales agree particularly well with the data.

Energies between 350 keV and 1 MeV exhibit a minimum in the loss timescales at around $L^* = 2-3$, with the location decreasing slightly with energy. This feature is captured by the model, even though an initial examination of Figure 1 shows the diffusion rates generally increase with L^* . However, if there is consistent diffusion from 90° to the loss cone, then the diffusion rate at the loss cone controls the rate of loss and hence the loss timescale. Figure 3 shows the pitch angle diffusion coefficient at the edge of the loss cone for energies from 100 keV (purple) to 1 MeV (red) as a function of L^* for the case when $1 \leq Kp < 2$. For 100 keV (purple) these diffusion rates increase to a maximum around $L^* = 4.5$ and then decrease slightly. For the higher energies, there is a peak between $L^* = 2.5-3.5$, with the lower L^* values corresponding to the higher energies. These peaks in

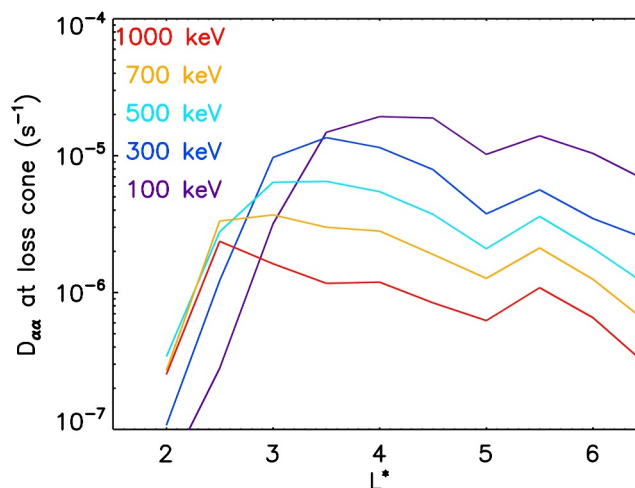


Figure 3. Pitch angle diffusion coefficients at the loss cone for $1 \leq Kp < 2$ and energies of 100 (purple), 300 (blue), 500 (cyan), 700 (orange) and 1,000 (red) keV.

the diffusion rates at the loss cone correspond well with the minima in the Claudepierre loss timescales, suggesting that in these cases the diffusion rate at the loss cone dominates in determining the loss timescale.

At intermediate energies ($350 \text{ keV} \leq E \leq 750 \text{ keV}$) in Figure 2, activity only has a modest effect on loss timescales, reducing them by less than an order of magnitude at higher L^* . However, at higher energies the decrease can be several orders of magnitude, probably due to the action of EMIC waves.

For $L^* < 3$ and energies below 1.5 MeV, the loss timescales in Figure 2 have little dependence on activity. Transmitters, LGW, and collisions are all effective in this region but their diffusion coefficients are independent of geomagnetic activity. Hiss only has limited activity dependence in this region, with the result that the combined diffusion coefficients for $L^* \leq 3$ (Figure 1) have little activity dependence.

For 2.6 MeV electrons in Figure 2 there is a local peak in the loss timescales around $L^* = 3.5$ for the two lowest activity levels that is not present in the data. The EMIC diffusion coefficients employed here are only defined for $L^* > 3.25$, but He et al. (2023) present evidence for EMIC waves in the inner radiation belt, so EMIC wave power may be missed at lower L^* . Alternatively, as this peak is present at low levels of activity it is unlikely to be due to chorus, but may be due to underestimating hiss, either because the hiss model does not include low frequency hiss (Ni et al., 2014) or does not account fully for variations in the wave-normal angle (Hartley et al., 2018).

3.1. Effects of Chorus, Magnetosonic Waves and LGW

Generally, Figure 2 shows that the loss timescales calculated from the diffusion coefficients in Figure 1 are in better agreement with the data than those presented by Claudepierre et al. (2020a). Claudepierre et al. (2020a) did not include chorus or magnetosonic waves in their loss timescale calculations and only account for lightning-generated whistlers in a way that they describe as ad hoc and that they speculate may not be rigorous enough. To examine the effect of these waves on the loss timescales, the calculations were repeated omitting each of these waves in turn. The results are shown in Figure 4, which reproduces parts of Figure 2 and adds corresponding plus signs to show the loss timescales when the diffusion due to a particular wave is removed from the calculation.

The top line (panels a–c) of Figure 4 illustrates the effect of omitting chorus waves from the calculation. For $1 \leq Kp < 2$ (purple) and $3 \leq Kp < 4$ (cyan) chorus activity reduces the loss timescale for $L^* > 4$ and improves the agreement with the data, suggesting that chorus wave activity is significant at these higher L^* even during quieter geomagnetic activity. This effect is largest around 743 keV.

The second line (panels d–f) in Figure 4 illustrates the effect of removing magnetosonic waves from the calculations. For most of the L^* , energy and activity levels, removing magnetosonic waves has no significant effect as the plus signs lie on the solid lines. The most noticeable exception is at $L^* = 3$ for 350 keV where the inclusion of magnetosonic waves reduces the loss timescale by a factor of about 3. At $L^* = 2$, the inclusion of magnetosonic waves has little significant effect. Wong et al. (2022) reported more significant reductions in loss timescales from the inclusion of magnetosonic waves. For example, their calculations showed reductions in the loss timescales by a factor of about 4 for 1 MeV electrons with $Kp = 4$ at $L^* = 2$, and by a factor of about 3.6 for 500 keV electrons at $L^* = 2.5$, again for $Kp = 4$. However, their calculations did not include diffusion due to LGW, which tends to dominate over the diffusion due to magnetosonic waves at low L^* .

The effect of removing LGW is shown in the bottom line (panels g–i) of Figure 4. LGW reduce the loss timescale of electrons at $L^* \leq 3$, with the largest effect, a reduction in the loss timescale by a factor of more than 5, seen at 700 keV at $L^* = 2$, suggesting it is important to include a realistic model of LGW at these low L^* .

4. Electron Pitch Angle Distributions

The aim of this work was to calculate PADs for use in radiation belt modeling, and the method of determining the loss timescale in Section 2 also provides the associated pitch angle distribution for each energy, L^* and geomagnetic activity level. Some examples of these are shown in Figure 5. Each panel shows the normalized PAD for quiet ($1 \leq Kp < 2$), intermediate ($3 \leq Kp < 4$), and disturbed ($5 \leq Kp < 6$) levels of activity in purple, cyan and yellow respectively. Different L^* values ($L^* = 2.5, 3.5, 4.5$ and 5.5) are shown across the page and selected electron energies (100, 500, 800 keV, 1, 2, and 4 MeV) are shown down the page. The dotted lines in the panels for 100, 500, and 800 keV show PADs determined from VAP data, taken from Allison et al. (2018). Note that the

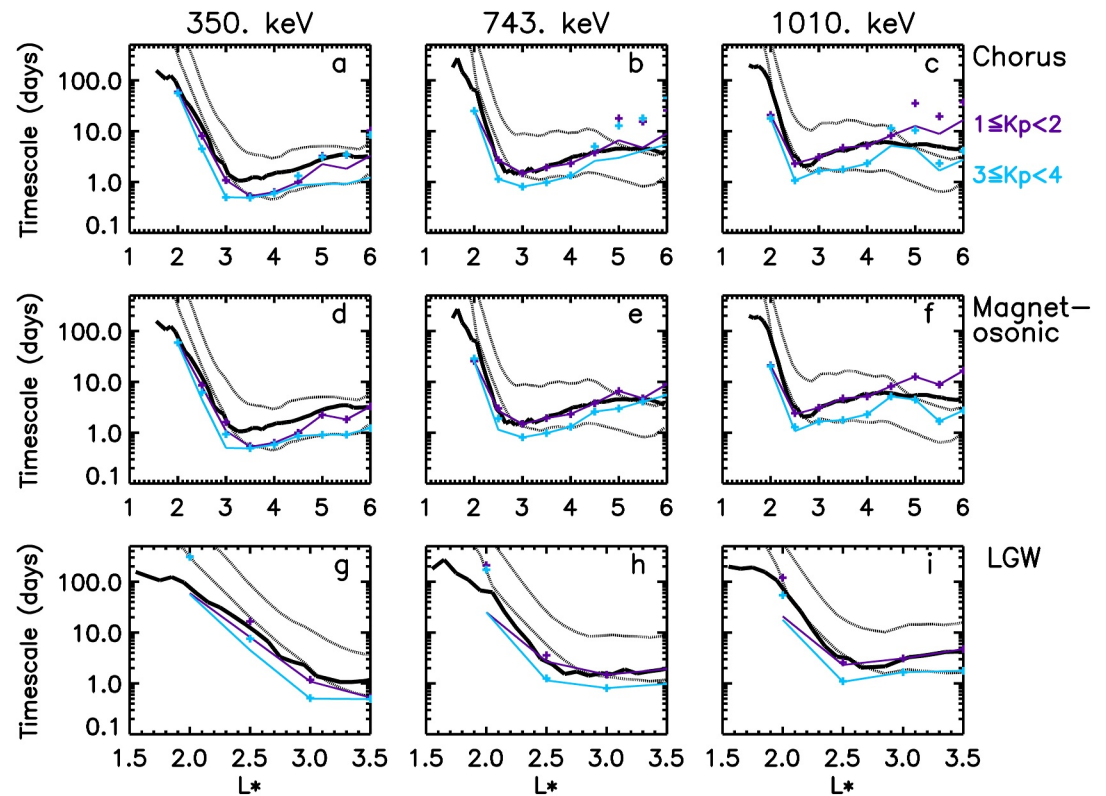


Figure 4. Electron loss timescales with (solid lines) and without (plus signs) the named wave as a function of L^* at the given energies. Panels a, b and c show electron loss timescales with and without chorus waves for energies of 350, 743 and 1,010 keV; panels d, e, and f show the effect of magnetosonic waves; panels g, h and i show the effect of LGW. The purple and cyan lines correspond to $1 \leq Kp < 2$ and $3 \leq Kp < 4$ respectively. The observational data from Claudepierre et al. (2020b) is shown in black and the upper and lower gray dotted lines are loss timescales calculated by Claudepierre et al. (2020a) for $Kp = 0$ and 5 respectively.

activity levels for the Allison et al. distributions are broader: the quiet range, $0 \leq Kp < 2$, is shown in purple intermediate activity, $2 \leq Kp \leq 4$, is in cyan and disturbed conditions for $Kp > 4$, are in yellow.

Above $L^* = 4$ and at energies above 100 keV and below 2 MeV, the profiles show very little activity dependence unlike the corresponding loss timescales. The pitch angle diffusion in this region is dominated by chorus which is efficient at moving electrons from 90° to the loss cone, with the lowest pitch angle diffusion coefficients occurring at the loss cone. The diffusion coefficients at a given energy and L^* have a similar shape but the magnitude increases with increasing geomagnetic activity, so increasing activity changes the loss timescale but has little effect on the shape of the distribution. This lack of activity dependence is consistent with Gu et al. (2011) who used CRRES data to show there is little change with activity at $L = 6.6$ at energies below 1 MeV for $Kp \leq 6$. Figure 5 is also consistent with Chen et al. (2014), who examined data from three satellites and found little activity dependence (defined by AE) in the PADs at $L = 4.2$ for energies from about 150 keV to 1.5 MeV.

For energies of 1 MeV and below, as L^* decreases the distributions become more peaked near 90° as hiss becomes the dominant wave. The hiss diffusion coefficients have a minimum at a pitch angle between about 45° and 80° , depending on energy and L^* , that results in electrons from near 90° diffusing slowly and dominating the decay rate (Meredith et al., 2009). This minimum is partially filled by LGW (Green et al., 2020) for $L^* \leq 3.0$ and transmitters (Ross et al., 2019) for $L^* \leq 2.5$. For example, when $1 \leq Kp < 2$, 500 keV electrons at $L^* = 4.5$ have a broad, flat top distribution that decreases rapidly near the loss cone. At $L^* = 3.5$, there is a narrow peak between about 80° and 90° that then falls gradually to the loss cone, while the PAD at $L^* = 2.5$ has a much more pronounced peak at 90° . At $L^* = 2.5$, there is a progression with increasing energy from peaked distributions at

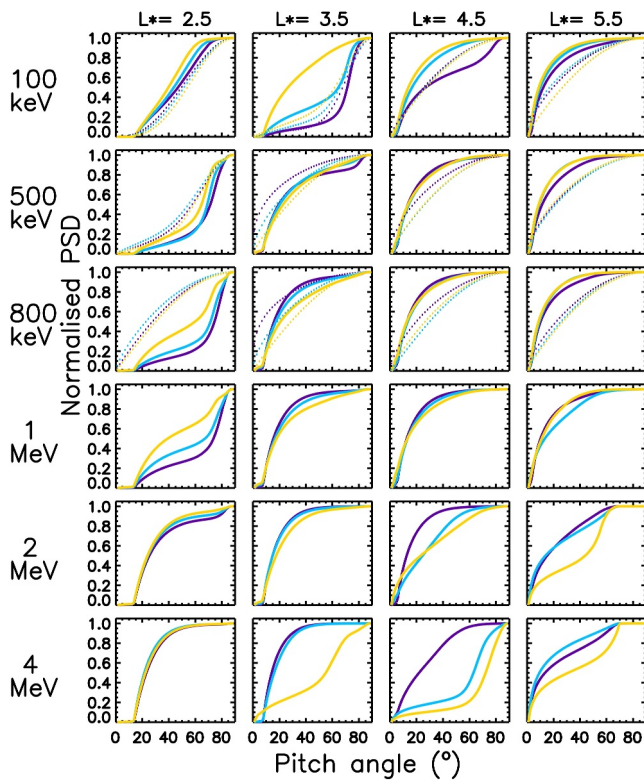


Figure 5. Normalized pitch angle distributions for $L^* = 2.5, 3.5, 4.5$ and 5.5 and energies of 100 keV, 500 keV, 800 keV, 1, 2 and 4 MeV. The solid lines show results from this work for $1 \leq Kp < 2$ (purple), $3 \leq Kp < 4$ (cyan), and $5 \leq Kp < 6$ (yellow). The dotted lines show distributions from Allison et al. (2018) for $0 \leq Kp < 2$ (purple), $2 \leq Kp < 4$ (cyan) and $Kp > 4$ (yellow).

500 keV to a much broader distribution at 4 MeV, as the minimum in the hiss diffusion coefficients gradually fills and electrons can diffuse from 90° at a much more constant rate.

For energies above 1 MeV and $L^* \geq 3.5$, the influence of EMIC waves is clear. With increasing activity and L^* , the distributions become increasingly peaked near 90° , consistent with observations in Ni et al. (2015), Zhao et al. (2018) and Greeley et al. (2021) (Note that the EMIC diffusion coefficients used here are only defined for $L^* \geq 3.25$.)

Allison et al. (2018) derive L^* , energy and Kp dependent PADs from Van Allen Probes data that can be compared with the PADs derived here. The Allison et al. (2018) PADs have the form

$$p(\alpha_0) = A \sin^{n1} \alpha_0 + (1 - A) \sin^{n2} \alpha_0 \quad (3)$$

with $0 \leq A \leq 1$, where the constants A , $n1$ and $n2$ were determined by a least-squares fit to normalized PADs.

For 100 and 500 keV, the PADs in Figure 5 show good agreement with PADs from Allison et al. (2018), shown in the figure as dotted lines. At these energies, and particularly at 100 keV, the largest differences occur for the highest activity levels, shown in yellow. The highest activity level in the Allison results is for $Kp > 4$, which will be dominated by Kp values around 4, so these results may provide a poor comparison for the more active conditions when $5 \leq Kp < 6$. The largest difference from the Allison et al. (2018) PADs occurs at 800 keV for $L^* = 2.5$. Here the Allison PADs still have significant values within the loss cone, even in quiet (purple) conditions, and the fits used a single sin function, so $A = 1$ with $n1 = 0.73$ for the lowest activity level. Shi et al. (2016) also fitted a single sin function to Van Allen Probes data, but had $n > 6$ for 600 keV electrons at $L^* = 2.5$. Although this energy is lower than the 800 keV discussed here, it suggests that the distribution may be more peaked than the Allison results suggest and the difference in Figure 5 may arise from the fitting of the data.

4.1. Effects of Chorus, Magnetosonic Waves and LGW on PADs

Analogous to Figures 4, Figure 6 illustrates the effect on the PADs of omitting chorus, LGW and magnetosonic waves. In some cases, removing the given wave can have a significant effect on the loss timescale but little effect on the PAD, for example, removing chorus for 700 keV electrons at $L^* = 5.5$ increases the loss timescale from 7 to 17 days for $2 \leq Kp < 3$, even though the PADs are very similar, see Figure 6, panel a. However, removing magnetosonic waves from the calculation at $L^* = 3$ for 500 keV electrons narrows the peak in the PAD but has no significant effect on the loss timescale for $4 \leq Kp < 5$, see Figure 6, panel d.

Omitting chorus from the calculation mainly affects the shape of the PAD for energies above 500 keV and $L^* > 5$, where the lack of chorus tends to make the distributions more peaked near 90° , with the effect becoming more pronounced as energy and activity increase, see panels a–c in Figure 6. These more peaked distributions are associated with longer lifetimes (see Figure 4, panels a–c), as there is a minimum in the other diffusion coefficients between about 30 and 60° that is filled in by the chorus diffusion coefficients.

Magnetosonic waves have the largest effect on the PAD around $L^* = 3$ and 500 keV, see panels d–f in Figure 6, where the waves broaden the distribution by partially filling a narrow minimum around 70 – 80° . A smaller effect can be seen at 800 keV and 1 MeV and at similar energies at lower L^* . This effect is most noticeable at high activity ($4 \leq Kp < 5$, shown in green), and is consistent with the results of Wong et al. (2022).

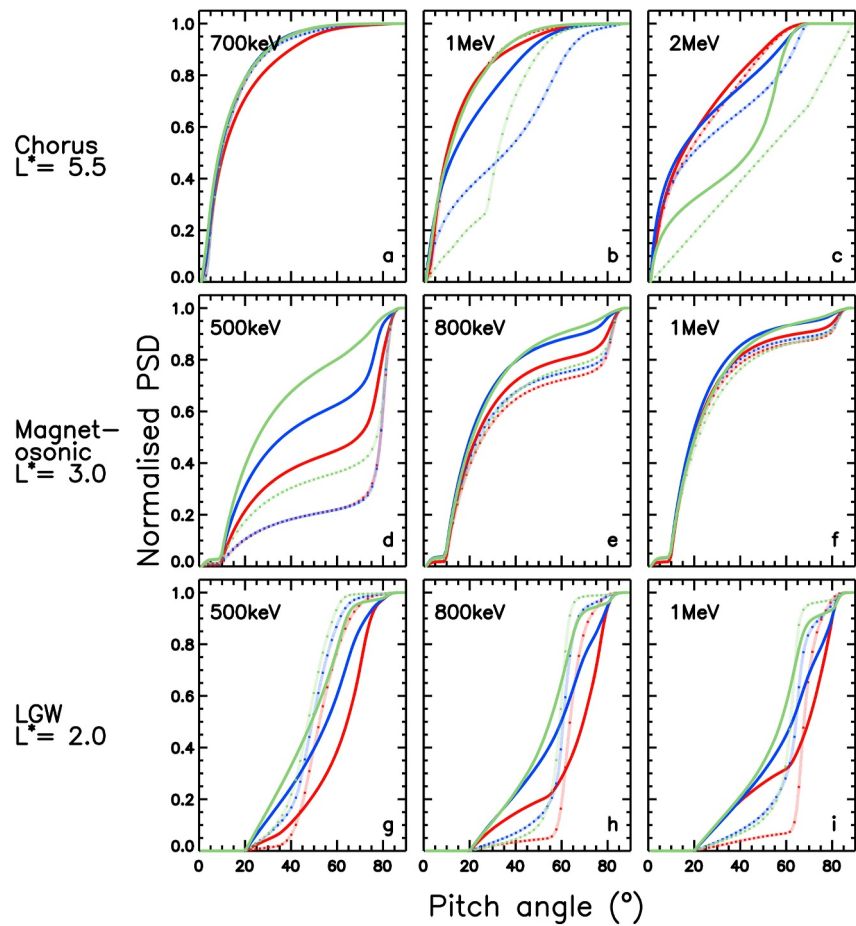


Figure 6. PADs with (solid line) and without (dashed line) the named wave as a function of L^* at the given energies. Panels a, b and c show PADs with and without chorus waves for energies of 700 keV, 1 and 2 MeV at $L^* = 5.5$; panels d, e, and f show the effect of magnetosonic waves for energies of 500 keV, 800 keV and 1 MeV at $L^* = 3.0$; panels g, h and i show the effect of LGW for energies of 500 keV, 800 keV and 1 MeV at $L^* = 2.0$. The red, blue and green lines are for $0 \leq Kp < 1$, $2 \leq Kp < 3$ and $4 \leq Kp < 5$ respectively.

Omitting LGW from the calculations also produces more peaked distributions, with the largest effect seen at $L^* = 2$, as shown in panels g–i of Figure 6. Particularly at energies between about 500 keV and 1 MeV, the distributions are strongly peaked near 90° , leading to much longer lifetimes at these L^* and energies, see Figure 4, panels g–i.

5. Discussion

Theoretical electron loss timescales and their associated PADs have been determined from a comprehensive set of diffusion coefficients for use in radiation belt models. These have been calculated using drift-average diffusion coefficients assuming pure pitch angle diffusion and neglecting the effects of energy diffusion, mixed pitch-angle and energy diffusion, and radial diffusion.

This approach neglects the effect of energy diffusion on the lifetimes and PADs. As chorus wave acceleration has been shown to have a significant effect on radiation belt dynamics (Horne, Thorne, Shprits, et al., 2005), this is likely to be most significant when chorus wave power is strong (Horne et al., 2013). Horne, Thorne, Glauert, et al. (2005) showed that an order of magnitude increase in the electron flux at 1 MeV takes about 1 day at $L = 4.5$ so the timescales for acceleration can be comparable to those derived here for electron loss. However, pitch angle and energy diffusion rates are related (Glauert & Horne, 2005), so significant energy diffusion generally coincides with increased pitch angle diffusion. If the energy diffusion is fairly constant with energy, then energy diffusion could potentially have little effect on the pitch angle distribution or even the loss timescale. For the L^* and

energies considered here, the steepest energy gradients in the chorus diffusion coefficients for active conditions occur at energies above 1 MeV, where pitch angle diffusion is rapid due to EMIC waves. Hence, at least at some energies and L^* , including energy diffusion may not significantly alter the results. Similarly, radial diffusion generally increases at all L^* simultaneously (Brautigam & Albert, 2000), so its influence on loss timescales and pitch angle distributions may, in some cases, be small. These effects can be investigated using 2- and 3-dimensional radiation belt models and this will be the subject of further work.

Cunningham (2023) suggests that, in certain situations, some of the assumptions underlying the calculation of diffusion coefficients by the PADIE code (Glauert & Horne, 2005) and similar codes may be improved. At low values of the ratio of the plasma frequency to the gyro frequency, $f_{pe}/f_{ce} = 1.5$, and at wave-normal angles very close to the resonance cone this can lead to significant differences in the local diffusion coefficients at some energies and pitch angles. While these result merit further study, it has yet to be demonstrated that the differences are significant once the diffusion coefficients have been bounce- and drift-averaged and the different wave modes combined. Further, the f_{pe}/f_{ce} used to calculate the chorus diffusion coefficients employed here are typically ≥ 3 , even in the most active conditions, and, unlike Cunningham (2023), these diffusion coefficient calculations reduce the wave power when the wave normal angle approaches the resonance cone to prevent the waves becoming electrostatic, see Horne et al. (2013). While the Cunningham result merits further study, it has yet to be demonstrated that the differences are significant once the diffusion coefficients have been bounce- and drift-averaged and the different wave modes combined. For the reasons above, it is unlikely that the differences demonstrated in Cunningham (2023) would substantially alter the results presented here, but this does need to be tested thoroughly elsewhere.

The results demonstrated here use drift-average diffusion coefficients so the pitch angle distributions do not have any MLT dependence. Various authors (Allison et al., 2017; Chen et al., 2019; Smirnov et al., 2022) have shown MLT asymmetries in the pitch angle distributions. Allison et al. (2017) showed dawn/dusk asymmetries in the flux for >30, >100 and >300 keV electrons that increased with activity and L^* . They were also noted by (Chen et al., 2019), particularly for $L \geq 6.5$. Ozeke et al. (2022) demonstrated that butterfly PADs occur preferentially on the night-side at higher L , as a result of magnetopause shadowing. The MLT asymmetries seen in these measurements make direct comparisons of the results presented here with observations challenging, particularly at higher L^* values and during more active conditions where the asymmetries are often stronger (Allison et al., 2017; Chen et al., 2019). Since simultaneous measurements around an electron drift path are not generally available, comparisons can only be done on a more statistical basis. Although the analysis presented here could be repeated using bounce-rather than drift-, averaged diffusion coefficients, some of the wave models (e.g., EMIC waves) are calculated without MLT dependence due to a lack of observations, so these wave models would need to be extended to include MLT dependence before MLT dependent PADs could be calculated. However, the applications that motivated this work require a drift-average PAD so MLT effects can be neglected.

The approach adopted here, assuming pure pitch angle diffusion, cannot reproduce butterfly PADs. These were reported by (Horne, Thorne, Glauert, et al., 2005) and their distribution has been studied by various authors, for example, (Chen et al., 2014; Greeley et al., 2021; Gu et al., 2011; Zhao et al., 2018). Their formation has been attributed to chorus waves (Horne, Thorne, Shprits, et al., 2005) and plasmaspheric hiss (Albert et al., 2016), as well as magnetopause shadowing (Ozeke et al., 2022) and drift-shell splitting (Roederer, 1970; Stone, 1963). To reproduce butterfly PADS from diffusion coefficients requires at least a 2-dimensional (pitch angle and energy) diffusion model. However, Ozeke et al. (2022) showed that overall butterfly PADS occurred much less frequently than non-butterfly PADS. Also, in 3-dimensional diffusion models, butterfly PADs may be reproduced as losses due to direct magnetopause shadowing occur first at the highest pitch angles (Glauert et al., 2014a).

The boundary conditions employed here assume very rapid diffusion in the loss cone (due to collisions) and loss to the atmosphere by imposing $f = 0$ at α_{\min} . These assumptions are reasonable as long as the strong diffusion limit (Kennel & Engelmann, 1966) is not reached. The diffusion coefficients used here are created by combining models for the different wave modes and none of the combined coefficients reach this limit. Strong diffusion has been observed but appears to be limited in space and time (Daggitt et al., 2024) and is likely to be associated with strong, short-lived bursts of chorus and EMIC waves. As the results presented here are averaged over an electron drift orbit and therefore represent a much longer timescale, the PADs and loss timescales are a reasonable approximation for use in drift-averaged models.

The theory used to derive the loss timescales and PADs, assumes that the system has decayed to the dominant eigenmode, that is, it has reached a state of steady decay. In practice, it will take a finite time for this to happen and the time taken for this to be the case will depend on the diffusion coefficient and the starting condition. The decay periods shown in Claudepierre et al. (2020b) and Meredith et al. (2006) generally don't show evidence of a two stage decay, suggesting that the steady decay is reached relatively quickly.

These results cover $2 \leq L^* \leq 7$. Although the chorus diffusion model extends out to $L^* = 9.5$, the model for EMIC waves is only defined for $3.25 \leq L^* \leq 7.0$. Grison et al. (2021) has shown that significant EMIC wave power exists at $L^* > 7$. Extending the EMIC diffusion coefficients into this region and calculating PADS here would be useful for working with the GPS (Morley et al., 2018) and Galileo observations. The lower limit $L^* = 3.25$ of the EMIC diffusion model is imposed by the limitations of the instruments used (Ross et al., 2020). He et al. (2023) present evidence for EMIC waves in the inner radiation belt during storms, so EMIC wave power may be missed at lower L^* . If this is the case, then the actual loss timescales for energies above 1 MeV at $L^* < 3.25$ during active periods may be faster than those presented here.

6. Summary and Conclusions

Theoretical pitch angle distributions and the associated timescales for electron loss have been calculated for electrons with energies between 100 keV and 5 MeV, $2 \leq L^* \leq 7$ with geomagnetic activity defined by the Kp index. The calculation includes the combined, drift-averaged effect of upper and lower band chorus waves, plasmaspheric hiss, lightning-generated whistlers, magnetosonic waves, EMIC waves and VLF transmitters. Our main conclusions are.

1. The modeled loss timescales show good agreement with VAP data during sustained periods of decay and the PADs agree well with previous results derived from data.
2. Chorus waves have a significant effect on electron loss timescales for $L^* \geq 4$, even during low levels of geomagnetic activity
3. Lightning-generated whistlers contribute significantly to losses at $L^* \leq 3$.
4. Magnetosonic waves only have a small effect on loss timescales over a limited range of L^* ($2.5 \leq L^* \leq 3$) when lightning-generated whistlers are included in the calculation.
5. When chorus is the dominant wave, the PADs are flat top distributions and have little activity dependence.
6. Plasmaspheric hiss and EMIC can both produce pancake distributions with a peak near 90° . PADs dominated by plasmaspheric hiss tend to broaden with activity, while those due to EMIC waves become more peaked with activity.

This work provides the comprehensive set of pitch angle distributions required to map low altitude measurements to the equatorial region in global radiation belt models.

Data Availability Statement

The Kp index was provided by OMNIWeb (<https://omniweb.gsfc.nasa.gov>). The diffusion coefficients, loss timescales and pitch angle distributions reported in this paper are available from the NERC EDS UK Polar Data Centre (<https://doi.org/10.5285/6d20ed7b-59e1-4284-a6f2-3e2589da6d2a>).

References

- Albert, J. M. (1994). Quasi-linear pitch angle diffusion coefficients: Retaining high harmonics. *Journal of Geophysical Research*, *99*(A12), 23741–23745. <https://doi.org/10.1029/94JA02345>
- Albert, J. M., Meredith, N. P., & Horne, R. B. (2009). Three-dimensional diffusion simulation of outer radiation belt electrons during the 9 October 1990 magnetic storm. *Journal of Geophysical Research*, *114*, A09214. <https://doi.org/10.1029/2009JA014336>
- Albert, J. M., & Shprits, Y. Y. (2009). Estimates of lifetimes against pitch angle diffusion. *Journal of Atmospheric and Solar-Terrestrial Physics*, *71*(16), 1647–1652. <https://doi.org/10.1016/j.jastp.2008.07.00>
- Albert, J. M., Starks, M. J., Horne, R. B., Meredith, N. P., & Glauert, S. A. (2016). Quasi-linear simulations of inner radiation belt electron pitch angle and energy distributions. *Geophysical Research Letters*, *43*(6), 2381–2388. <https://doi.org/10.1002/2016GL067938>
- Allison, H. J., Horne, R., Glauert, S., & Del Zanna, G. (2017). The magnetic local time distribution of energetic electrons in the radiation belt region. *Journal of Geophysical Research*, *122*(8), 8108–8123. Retrieved from <https://doi.org/10.1002/2017JA024084>
- Allison, H. J., Horne, R., Glauert, S., & Del Zanna, G. (2018). Determination of the equatorial electron differential flux from observations at low earth orbit. *Journal of Geophysical Research*, *123*(11), 9574–9596. Retrieved from <https://doi.org/10.1029/2018JA025786>

Acknowledgments

SG, JA, JR and RH were supported by NERC grant NE/V00249X/1 (Sat-Risk). SG and RH was also supported by NERC National Capability grant NE/R016038/1 and by NERC National Public Good activity grant NE/R016445/1.

- Aryan, H., Agapitov, O. V., Artemyev, A., Mourenas, D., Balikhin, M. A., Boynton, R., & Bortnik, J. (2020). Outer radiation belt electron lifetime model based on combined Van Allen Probes and Cluster VLF measurements. *Journal of Geophysical Research*, *125*(8), e2020JA028018. <https://doi.org/10.1029/2020JA028018>
- Baker, D. N. (2001). Satellite anomalies due to space storms. In I. A. Daglis (Ed.), *Space storms and space weather hazards* (p. 251). Springer. <https://doi.org/10.1007/978-94-010-0983-6>
- Baker, D. N., Kanekal, S. G., Horne, R. B., Meredith, N. P., & A. G. S. (2007). Low-altitude measurements of 2 – 6 MeV electron trapping lifetimes at $1.5 < L < 2.5$. *Geophysical Research Letters*, *34*, L20110. <https://doi.org/10.1029/2007GL031007>
- Baker, D. N., Li, X., Turner, N., Allen, J. H., Bargatze, L. F., Blake, J. B., et al. (1997). Recurrent geomagnetic storms and relativistic electron enhancements in the outer magnetosphere: ISTP coordinated measurements. *Journal of Geophysical Research*, *102*(A7), 14141–14148. <https://doi.org/10.1029/97JA00565>
- Brautigam, D. H., & Albert, J. M. (2000). Radial diffusion analysis of outer radiation belt electrons during the October 9, 1990, magnetic storm. *Journal of Geophysical Research*, *105*(A1), 291–309. <https://doi.org/10.1029/1999JA900344>
- Chen, Y., Friedel, R. H. W., Henderson, M. G., Claudepierre, S. G., Morley, S. K., & Spence, H. (2014). Repad: An empirical model of pitch angle distributions for energetic electrons in the Earth's outer radiation belt. *Journal of Geophysical Research*, *119*(3), 1693–1708. <https://doi.org/10.1002/2013ja019431>
- Chen, Y., Reeves, G. D., Fu, X., & Henderson, M. (2019). PreMeV-E: New predictive model for mega-electron-volt electrons inside Earth's outer radiation belt. *Space Weather*, *17*(3), 438–454. <https://doi.org/10.1029/2018SW002095>
- Claudepierre, S. G., Ma, Q., Bortnik, J., O'Brien, T. P., Fennell, J. F., & Blake, J. B. (2020a). Empirically estimated electron lifetimes in the earth's radiation belts: Comparison with theory. *Geophysical Research Letters*, *47*(3), e2019GL086056. <https://doi.org/10.1029/2019GL086056>
- Claudepierre, S. G., Ma, Q., Bortnik, J., O'Brien, T. P., Fennell, J. F., & Blake, J. B. (2020b). Empirically estimated electron lifetimes in the Earth's radiation belts: Van Allen Probe observations. *Geophysical Research Letters*, *47*(3), e2019GL0. <https://doi.org/10.1029/2019GL086053>
- Cunningham, G. S. (2023). Resolution of a few problems in the application of quasilinear theory to calculating diffusion coefficients in heliophysics. *Journal of Geophysical Research*, *128*(10), e2023JA031703. <https://doi.org/10.1029/2023JA031703>
- Daggitt, T. A., Horne, R. B., Glauert, S. A., Del Zanna, G., & Albert, J. M. (2024). Chorus wave power at the strong diffusion limit overcomes electron losses due to strong diffusion. *Nature Communications*, *15*(1), 1800. <https://doi.org/10.1038/s41467-024-45967-9>
- Glauert, S. A., & Horne, R. B. (2005). Calculation of pitch angle and energy diffusion coefficients with the PADIE code. *Journal of Geophysical Research*, *110*(A4), 1–15. <https://doi.org/10.1029/2004JA010851>
- Glauert, S. A., Horne, R. B., & Kirsch, P. (2021). Evaluation of SaRIF high-energy electron reconstructions and forecasts. *Space Weather*, *19*, e2021SW0. <https://doi.org/10.1029/2021SW002822>
- Glauert, S. A., Horne, R. B., & Meredith, N. P. (2014a). Simulating the Earth's radiation belts: Internal acceleration and continuous losses to the magnetopause. *Journal of Geophysical Research*, *119*(9), 7444–7463. <https://doi.org/10.1002/2014JA020092>
- Glauert, S. A., Horne, R. B., & Meredith, N. P. (2014b). Three dimensional electron radiation belt simulations using the BAS Radiation Belt Model with new diffusion models for chorus, plasmaspheric hiss and lightning-generated whistlers. *Journal of Geophysical Research*, *119*(1), 268–289. <https://doi.org/10.1002/2013JA019281>
- Glauert, S. A., Horne, R. B., & Meredith, N. P. (2018). A 30-year simulation of the outer electron radiation belt. *Space Weather*, *16*(16), 1498–1522. <https://doi.org/10.1029/2018SW001981>
- Greeley, A. D., Kanekal, S. G., Sibeck, D. G., Schiller, Q., & Baker, D. N. (2021). Evolution of pitch angle distributions of relativistic electrons during geomagnetic storms: Van Allen Probes Observations. *Journal of Geophysical Research*, *126*(2), e2020JA028335. <https://doi.org/10.1029/2020JA028335>
- Green, A., Li, W., Ma, Q., Shen, X., Bortnik, J., & Hospodarsky, G. B. (2020). Properties of lightning generated whistlers based on Van Allen Probes observations and their global effects on radiation belt electron loss. *Geophysical Research Letters*, *47*(17), e2020GL0. <https://doi.org/10.1029/2020GL089584>
- Grison, B., Santolík, O., Lukačević, J., & Usanova, M. E. (2021). Occurrence of emic waves in the magnetosphere according to their distance to the magnetopause. *Geophysical Research Letters*, *48*(3), e2020GL090921. <https://doi.org/10.1029/2020gl090921>
- Gu, X., Shprits, Y. Y., & Ni, B. (2012). Parameterized lifetime of radiation belt electrons interacting with lower-band and upper-band oblique chorus waves. *Geophysical Research Letters*, *39*, L15102. <https://doi.org/10.1029/2012GL052519>
- Gu, X., Zhao, Z., Ni, B., Shprits, Y., & Zhou, C. (2011). Statistical analysis of pitch angle distribution of radiation belt energetic electrons near the geostationary orbit: CRRES observations. *Journal of Geophysical Research*, *116*, A01208. <https://doi.org/10.1029/2010JA016052>
- Hartley, D. P., Kletzing, C. A., Santolík, O., Chen, L., & Horne, R. B. (2018). Statistical properties of plasmaspheric hiss from Van Allen Probes observations. *Journal of Geophysical Research*, *123*(4), 2605–2619. <https://doi.org/10.1002/2017JA024593>
- He, Z., Xu, J., Wang, C., Dai, L., Ni, B., & Roth, I. (2023). Evidence of h+ band emic waves in the inner radiation belt observed by van allen probes during magnetic storms. *Journal of Geophysical Research*, *128*(3), e2022JA031088. <https://doi.org/10.1029/2022JA031088>
- Horne, R. B., Kersten, T., Glauert, S. A., Meredith, N. P., Boscher, D., Sicard-Piet, A., et al. (2013). A new diffusion matrix for whistler mode chorus waves. *Journal of Geophysical Research*, *118*(10), 6302–6318. <https://doi.org/10.1002/jgra.50594>
- Horne, R. B., Meredith, N. P., Glauert, S. A., & Kersten, T. (2016). Wave driven diffusion in radiation belt dynamics. In G. Balasis, I. A. Daglis, & I. R. Mann (Eds.), *Waves, particles, and storms in geospace: A complex interplay* (pp. 217–243). Oxford University Press. <https://doi.org/10.1093/acprof:oso/9780198705246.001.0001>
- Horne, R. B., & Pitchford, D. (2015). Space weather concerns for all-electric propulsion satellites. *Space Weather*, *13*(8), 430–433. <https://doi.org/10.1002/2015SW001198>
- Horne, R. B., & Thorne, R. M. (1998). Potential waves for relativistic electron scattering and stochastic acceleration during magnetic storms. *Geophysical Research Letters*, *25*(15), 3011–3014. <https://doi.org/10.1029/98GL01002>
- Horne, R. B., Thorne, R. M., Glauert, S. A., Albert, J. M., Meredith, N. P., & Anderson, R. R. (2005). Timescale for radiation belt electron acceleration by whistler mode chorus waves. *Journal of Geophysical Research*, *110*(A3), A03225. <https://doi.org/10.1029/2004JA010811>
- Horne, R. B., Thorne, R. M., Shprits, Y. Y., Meredith, N. P., Glauert, S. A., Smith, A. J., et al. (2005). Wave acceleration of electrons in the Van Allen radiation belts. *Nature*, *437*(7056), 227–230. <https://doi.org/10.1038/nature03939>
- Jaynes, A. N., Baker, D. N., Singer, J. V., Rodriguez, J. V., Loto'aniu, T. M., Ali, A. F., et al. (2015). Source and seed populations for relativistic electrons: Their roles in radiation belt changes. *Journal of Geophysical Research*, *120*(9), 7240–7254. <https://doi.org/10.1002/2015JA021234>
- Kennel, C. F., & Engelmann, F. (1966). Velocity space diffusion from weak plasma turbulence in a magnetic field. *Physics of Fluids*, *9*(12), 2377–2388. <https://doi.org/10.1063/1.1761629>
- Lyons, L. R. (1974). General relations for resonant particle diffusion in pitch angle and energy. *Journal of Plasma Physics*, *12*(AUG), 45–49. <https://doi.org/10.1017/s0022377800024910>

- Lyons, L. R., Thorne, R. M., & Kennel, C. F. (1972). Pitch-angle diffusion of radiation belt electrons within the plasmasphere. *Journal of Geophysical Research*, 77(19), 3455–3474. <https://doi.org/10.1029/JA077i019p03455>
- Meredith, N. P., Horne, R. B., Glauert, S. A., Baker, D. N., Kanekal, S. G., & Albert, J. M. (2009). Relativistic electron loss timescales in the slot region. *Journal of Geophysical Research*, 114, A03222. <https://doi.org/10.1029/2008JA013889>
- Meredith, N. P., Horne, R. B., Glauert, S. A., Thorne, R. M., Summers, D., Albert, J. M., & Anderson, R. R. (2006). Energetic outer zone electron loss timescales during low geomagnetic activity. *Journal of Geophysical Research*, 111, A05212. <https://doi.org/10.1029/2005JA011516>
- Meredith, N. P., Horne, R. B., Kersten, T., Li, W., Bortnik, J., Sicard, A., & Yearby, K. H. (2018). Global model of plasmaspheric hiss from multiple satellite observations. *Journal of Geophysical Research*, 123(6), 4526–4541. <https://doi.org/10.1029/2018JA025226>
- Meredith, N. P., Horne, R. B., Shen, X., Li, W., & Bortnik, J. (2020). Global model of whistler mode chorus in the near-equatorial region ($|\lambda_m| < 18$). *Geophysical Research Letters*, 47(11), e2020GL087311. <https://doi.org/10.1029/2020GL087311>
- Morley, S. K., Sullivan, J. P., Henderson, M. G., Blake, J. B., & Baker, D. N. (2018). The Global Positioning System constellation as a space weather monitor: Comparison of electron measurements with Van Allen Probes data. *Space Weather*, 14(2), 76–92. <https://doi.org/10.1002/2015SW001339>
- Ni, B., Li, W., Thorne, R., Bortnik, J., Ma, Q., Chen, L., et al. (2014). Resonant scattering of energetic electrons by unusual low frequency hiss. *Geophysical Research Letters*, 41(6), 1854–1861. <https://doi.org/10.1002/2014gl059389>
- Ni, B., Zou, Z., Gu, X., Zhou, C., Thorne, R. M., Bortnik, J., et al. (2015). Variability of the pitch angle distribution of radiation belt ultrarelativistic electrons during and following intense geomagnetic storms: Van Allen Probes observations. *Journal of Geophysical Research*, 120(6), 4863–4876. <https://doi.org/10.1002/2015JA021065>
- Olson, W. P., & Pfizter, K. A. (1977). *Magnetospheric magnetic field modeling*. McDonnell Douglas Astronautics Co., Huntington Beach.
- Orlova, K., & Shprits, Y. (2014). Model of lifetimes of the outer radiation belt electrons in a realistic magnetic field using realistic chorus wave parameters. *Journal of Geophysical Research: Space Physics*, 119(2), 770–780. <https://doi.org/10.1002/2013JA019596>
- Orlova, K., Shprits, Y., & Spasojevic, M. (2016). New global loss model of energetic and relativistic electrons based on Van Allen Probes measurements. *Journal of Geophysical Research: Space Physics*, 121(2), 1308–1314. <https://doi.org/10.1002/2015JA021878>
- Ozeke, L., Mann, I., Murphy, K., Degeling, A. W., Claudepierre, S. G., & Spence, H. E. (2018). Explaining the apparent impenetrable barrier to ultra-relativistic electrons in the outer Van Allen belt. *Nature Communications*, 9(1844), 1844. <https://doi.org/10.1038/s41467-018-04162-3>
- Ozeke, L., Mann, I., Olifer, L., Claudepierre, S., Spence, H., & Baker, D. (2022). Statistical characteristics of energetic electron pitch angle distributions in the van allen probe era: 1. Butterfly distributions with flux peaks at preferred pitch angles. *Journal of Geophysical Research: Space Physics*, 127(3), e2021JA029907. <https://doi.org/10.1029/2021JA029907>
- Ozhogin, P. J., Tu, P. S., & Reinisch, B. W. (2012). Field-aligned distribution of the plasmaspheric electron density: An empirical model derived from the IMAGE RPI measurements. *Journal of Geophysical Research*, 117(117), A06225. <https://doi.org/10.1029/2011JA017330>
- Reeves, G. D., Friedel, R. H. W., Larsen, B. A., Skoug, R. M., Funsten, H. O., Claudepierre, S. G., et al. (2016). Energy-dependent dynamics of keV to MeV electrons in the inner zone, outer zone, and slot regions. *Journal of Geophysical Research*, 121(1), 397–412. <https://doi.org/10.1002/2015ja021569>
- Reeves, G. D., McAdams, K. L., Friedel, R. H. W., & O'Brien, T. P. (2003). Acceleration and loss of relativistic electrons during geomagnetic storms. *Geophysical Research Letters*, 30(10), 1529. <https://doi.org/10.1029/2002GL016513>
- Reidy, J. A., Horne, R. B., Glauert, S. A., Clilverd, M. A., Meredith, N. P., Woodfield, E. E., et al. (2021). Comparing electron precipitation fluxes calculated from pitch angle diffusion coefficients to LEO satellite observations. *Journal of Geophysical Research: Space Physics*, 126(3), e2020JA028410. <https://doi.org/10.1029/2020JA028410>
- Ripoll, J.-F., Chen, Y., Fennell, J. F., & Friedel, R. H. W. (2015). On long decays of electrons in the vicinity of the slot region observed by HEO3. *Journal of Geophysical Research*, 120(1), 460–478. <https://doi.org/10.1002/2014JA020449>
- Roederer, J. G. (1970). *Dynamics of geomagnetically trapped radiation*. Springer. <https://doi.org/10.1007/978-3-642-49300-3>
- Ross, J. P. J., Glauert, S. A., Horne, R. B., Watt, C. E., Meredith, N. P., & Woodfield, E. E. (2020). A new approach to constructing models of electron diffusion by EMIC waves in the radiation belts. *Journal of Geophysical Research*, 47(20), e2020GL088976. <https://doi.org/10.1029/2020GL088976>
- Ross, J. P. J., Glauert, S. A., Horne, R. B., Watt, C. E. J., & Meredith, N. P. (2021). On the variability of EMIC waves and the consequences for the relativistic electron radiation belt population. *Journal of Geophysical Research*, 126(12), e2021JA029754. <https://doi.org/10.1029/2021JA029754>
- Ross, J. P. J., Meredith, N. P., Glauert, S. A., Horne, R. B., & Clilverd, M. A. (2019). Effects of VLF transmitter waves on the inner belt and slot region. *Journal of Geophysical Research: Space Physics*, 124(7), 5260–5277. <https://doi.org/10.1029/2019JA026716>
- Schulz, M., & Lanzerotti, L. J. (1974). *Particle diffusion in the radiation belts*. Springer-Verlag. <https://doi.org/10.1007/978-3-642-65675-0>
- Selesnick, R. S. (2016). Stochastic simulation of inner radiation belt electron decay by atmospheric scattering. *Journal of Geophysical Research*, 121(2), 1249–1262. <https://doi.org/10.1002/2015JA022180>
- Shi, R., Summers, D., Ni, B., Fennell, J. F., Blake, J. B., Spence, H. E., & Reeves, G. D. (2016). Survey of radiation belt energetic electron pitch angle distributions based on the Van Allen Probes MagEIS measurements. *Journal of Geophysical Research*, 121(121), 1078–1090. <https://doi.org/10.1002/2015JA021724>
- Shprits, Y. Y., Li, W., & Thorne, R. M. (2006). Controlling effect of the pitch angle scattering rates near the edge of the loss cone on electron lifetimes. *Journal of Geophysical Research*, 111, A12206. <https://doi.org/10.1029/2006JA011758>
- Shprits, Y. Y., Meredith, N. P., & Thorne, R. M. (2007). Parameterization of radiation belt electron loss timescales due to interactions with chorus waves. *Geophysical Research Letters*, 34, L11110. <https://doi.org/10.1029/2006GL029050>
- Shprits, Y. Y., & Thorne, R. M. (2004). Time dependent radial diffusion modeling of relativistic electrons with realistic loss rates. *Geophysical Research Letters*, 31(8), L08805. <https://doi.org/10.1029/2004GL019591>
- Smirnov, A., Shprits, Y., Allison, H. J., Aseev, N., Drozdov, A., Kollmann, P., et al. (2022). Storm-time evolution of the equatorial electron pitch angle distributions in earth's outer radiation belt. *Frontiers in Astronomy and Space Sciences*, 9, 836811. <https://doi.org/10.3389/fspas.2022.836811>
- Stone, E. C. (1963). The physical significance and application of l , b_0 , and r_0 to geomagnetically trapped particles. *Journal of Geophysical Research*, 68(14), 4157–4166. <https://doi.org/10.1029/JZ068i014p04157>
- Subbotin, D., Shprits, Y., & Ni, B. (2010). Three-dimensional VERB radiation belt simulations including mixed diffusion. *Journal of Geophysical Research*, 115, A03205. <https://doi.org/10.1029/2009JA015070>
- Summers, D., Ma, C., Meredith, N. P., Horne, R. B., Thorne, R. M., Heynderickx, D., & Anderson, R. R. (2002). Model of the energization of outer-zone electrons by whistler-mode chorus during the October 9, 1990 geomagnetic storm. *Geophysical Research Letters*, 29(24), 2174. <https://doi.org/10.1029/2002GL016039>

- Tu, W., Cunningham, G. S., Chen, Y., Henderson, M. G., Camporeale, E., & Reeves, G. D. (2013). Modeling radiation belt electron dynamics during GEM challenge intervals with the DREAM3D diffusion model. *Journal of Geophysical Research*, *118*(10), 6197–6211. <https://doi.org/10.1002/jgra.50560>
- Wong, J., Meredith, N. P., Horne, R. B., Glauert, S. A., & Ross, J. (2022). Electron diffusion by magnetosonic waves in the Earth's radiation belts. *Journal of Geophysical Research: Space Physics*, *127*(4), e2021JA030196. <https://doi.org/10.1029/2021JA030196>
- Wrenn, G. L., Rodgers, D. J., & Ryden, K. A. (2002). A solar cycle of spacecraft anomalies due to internal charging. *Annals of Geophysics*, *20*(7), 953–956. <https://doi.org/10.5194/angeo-20-953-2002>
- Zhao, H., Friedel, R. H. W., Chen, Y., Reeves, G. D., Baker, D. N., Li, X., et al. (2018). An empirical model of radiation belt electron pitch angle distributions based on Van Allen Probes measurements. *Journal of Geophysical Research*, *123*(5), 3493–3511. <https://doi.org/10.1029/2018JA025277>